NeuroImage: Clinical 9 (2015) 58–68

Contents lists available at ScienceDirect

NeuroImage: Clinical

journal homepage: www.elsevier.com/locate/ynicl

High-field magnetic resonance imaging of the human temporal lobe☆

Luis M. Colon-Perez [a,b,*], Michael King [c,d], Mansi Parekh [e], Angelique Boutzoukas [f], Eduardo Carmona [g], Michelle Couret [h], Rosemary Klassen [i], Thomas H. Mareci [a], Paul R. Carney [j,k,l,m,**]

[a] Department of Biochemistry and Molecular Biology, University of Florida, Gainesville, FL, USA
[b] Department of Psychiatry, University of Florida, Gainesville, FL, USA
[c] Department of Pharmacology and Therapeutics, University of Florida, Gainesville, FL, USA
[d] Department of Veterans Affairs Medical Center, Gainesville, FL, USA
[e] Department of Radiology, Stanford University, Stanford, CA, USA
[f] Department of Medicine, University of Florida, Gainesville, FL, USA
[g] Department of Biology, University of Florida, Gainesville, FL, USA
[h] Department of Chemistry, University of Florida, Gainesville, FL, USA
[i] Department of Psychology, University of Florida, Gainesville, FL, USA
[j] Department of Neurology, University of Florida, Gainesville, FL, USA
[k] Department of Pediatrics, University of Florida, Gainesville, FL, USA
[l] Department of Neuroscience, University of Florida, Gainesville, FL, USA
[m] J. Crayton Family Department of Biomedical Engineering, University of Florida, Gainesville, FL, USA

ARTICLE INFO

Article history:
Received 13 March 2015
Received in revised form 29 June 2015
Accepted 6 July 2015
Available online 1 August 2015

Keywords:
High-field MRI
DWI
Ex vivo brain imaging
Tractography
Mesoscale structure

ABSTRACT

Background: Emerging high-field diffusion weighted MR imaging protocols, along with tractography, can elucidate microstructural changes associated with brain disease at the sub-millimeter image resolution. Epilepsy and other neurological disorders are accompanied by structural changes in the hippocampal formation and associated regions; however, these changes can be subtle and on a much smaller scale than the spatial resolution commonly obtained by current clinical magnetic resonance (MR) protocols *in vivo*.
Methods: We explored the possibility of studying the organization of fresh tissue with a 17.6 Tesla magnet using diffusion MR imaging and tractography. The mesoscale organization of the temporal lobe was estimated using a fresh unfixed specimen obtained from a subject who underwent anterior temporal lobectomy for medically refractory temporal lobe epilepsy (TLE). Following *ex vivo* imaging, the tissue was fixed, serial-sectioned, and stained for correlation with imaging.
Findings: We resolved tissue microstructural organizational features in the temporal lobe from diffusion MR imaging and tractography in fresh tissue.
Conclusions: Fresh *ex vivo* MR imaging, along with tractography, revealed complex intra-temporal structural variation corresponding to neuronal cell body layers, dendritic fields, and axonal projection systems evident histologically. This is the first study to describe in detail the human temporal lobe structural organization using high-field MR imaging and tractography. By preserving the 3-dimensional structures of the hippocampus and surrounding structures, specific changes in anatomy may inform us about the changes that occur in TLE in relation to the disease process and structural underpinnings in epilepsy-related memory dysfunction.

1. Introduction

Sub-millimeter resolution magnetic resonance (MR) imaging has been proposed as a tool for the study of volumetric changes in the subfields of hippocampal formations in neuropsychiatric and degenerative diseases (Wisse et al., 2012; Yushkevich et al., 2010). Epilepsy is one of the most common neurological disorders in humans, afflicting more than 65 million people worldwide (England et al., 2012). Over 30% of patients have seizures refractory to commonly used anti-convulsant drugs (Bauer and Burr, 2001). The most common form of epilepsy is temporal lobe epilepsy (TLE) and mesial temporal lobe

* Correspondence to: L.M. Colon-Perez, 1149 SW Newell Dr. L4-100, Gainesville, FL 32610, USA.
** Correspondence to: P.R. Carney, 1600 SW Archer Road, PO Box 100296, Gainesville, FL 32610, USA.
E-mail address: carnepr@peds.ufl.edu (P.R. Carney).

http://dx.doi.org/10.1016/j.nicl.2015.07.005

sclerosis is the most common pathological abnormality in TLE (Bronen et al., 1997). The histopathological hallmarks of hippocampal sclerosis include loss of pyramidal neurons, granule cell dispersion, and reactive gliosis (Kienzler et al., 2009; Sutula et al., 1989). Recent advances in neuroimaging have demonstrated macroscale white matter abnormalities in TLE (Concha et al., 2005, 2009; Gross, 2011; Liu et al., 2012, 2014). Changes in the integrity of the hippocampus and white matter surrounding it have been postulated to influence overall temporal lobe network connectivity, hippocampal efficiency (Cadotte et al., 2009), and memory function (Eichenbaum et al., 2007, 2012; Liao et al., 2011a,b). Sub-millimeter highly resolved MR imaging may contribute to the study of these changes in brain structure and re-organization in brain tissue in disease.

The cytoarchitectonic features of nervous tissue and cellular organization influences how water diffuses in the brain (Beaulieu, 2002). For this reason, diffusion tensor imaging is becoming the standard magnetic resonance (MR) method for studying white matter *in vivo* and non-invasively (Hagmann et al., 2006). Diffusion MR imaging has shown promise as a diagnostic tool because it describes microstructural changes much earlier than structural scans, such as fluid-attenuated inversion recovery (FLAIR) (Gerdes et al., 2014) and subtle structural changes due to apoptosis and inflammation (Johnson et al., 2014). *In vivo* diffusion MR imaging protocols at 3 Tesla (T) magnets are limited by the image resolution achievable at this field strength, which restricts the accurate estimation of white matter nervous tissue structure to large fiber tracts (Cammoun et al., 2012; Hagmann et al., 2008). Volume averaging with large voxels (>1 mm^3) precludes resolution of finer internal anatomical organization. Hence, current *in vivo* diffusion MR imaging approaches are unable to discriminate the defining structural pathological changes of TLE, such as mossy fiber sprouting, loss of CA1 and dentate gyrus neurons in mesial temporal sclerosis and fimbria, and perforant pathway injury (Kienzler et al., 2009; Parekh et al., 2010). High-resolution structural information of the human brain therefore would be a useful approach to study these changes and to test anatomical predictions derived from animal pathway tracing studies (Amaral et al., 2014; Oh et al., 2014; Silasi and Murphy, 2014). However, diffusion MR imaging at sub-millimeter isotropic image resolution is rarely feasible in current clinical MR scanners.

Developing improved high-resolution MR methods can be facilitated by the use of *ex vivo* tissue from individuals undergoing resective surgery for intractable epilepsy. The impact of high-resolution diffusion MR imaging over volumetric studies (Wisse et al., 2012) lies in its ability to provide sufficient contrast in order to identify sub-millimeter fields within tissues (Shepherd et al., 2007). Fresh tissue specimens with undisturbed internal cytoarchitecture can be subjected to protracted high-resolution imaging approaches currently unattainable *in vivo*. Long *ex vivo* acquisition times can yield high spatial resolution images with sufficient information to study small structures that may provide important information about the etiology, evolution, and progression of epilepsy. Both hippocampal subfield and temporal lobe structural analyses may produce more sensitive markers for epilepsy and neuropsychiatric disorders than whole-hippocampal volumetric analysis, especially early in disease. Therefore, such information is important for studies of brain pathology and in making decisions in clinical practice.

The brain is typically described on three scales: microscale, mesoscale, and macroscale (Silasi and Murphy, 2014; Sporns et al., 2005). Microscale refers to cellular features, mesoscale refers to neuronal group connections, and macroscale refers to the features of large anatomical brain regions. Particular interest is drawn to the mesoscale, with which great advances have been made using anterograde tracers (Amaral et al., 2014; Oh et al., 2014; Silasi and Murphy, 2014). MR imaging can be a great tool to assess mesoscale structure in the human brain by using tissue resected from patients undergoing treatment for epilepsy (Silasi and Murphy, 2014). In this study, a high-angular resolution diffusion imaging (HARDI) sequence was employed with micrometer scale spatial-resolution to estimate the mesoscale organization of the temporal lobe in an individual with pharmacoresistant TLE. This report describes 1) high-field (17.6) MR imaging as a tool for the study of mesoscale organization of freshly resected tissue resected from an epileptic patient, 2) qualitative validation of MR imaging with conventional histology, 3) interpretations of diffusion MR imaging and tractography, and 4) utility of streamline tractography for the study of mesoscale brain structure.

2. Methods

2.1. Participant information

The University of Florida Institutional Review Board approved this study. The patient is a 10-year-old right-handed boy who came to University of Florida Health Center hospital, a high complexity epilepsy center of excellence, in July 2010 because of a new onset status epilepticus. His seizures began with left-sided manual and oral automatisms, which then progressed to left arm and leg tonic/clonic seizures and left-sided head and eye deviation. He was started on oxycarbamazepine, which he remained on for 9 months. Over the ensuing months, his seizures recurred at every 2-week interval with each seizure lasting between 45 s and 1 min. His antiepileptic medication treatment was changed to lamotrigine, and clonazepam was later added. Subsequently, his seizure occurrence decreased to every 4–6 weeks. Topiramate and levetiracetam were later added to no avail. Surface electroencephalography showed right temporal lobe epileptiform discharges with right focal temporal region theta slowing. The patient was deemed medically intractable or drug resistant and therefore evaluated for resective epilepsy surgery. Phase one right electroencephalography showed posterior temporal and right parietal sharp epileptiform discharges. A phase two right temporal lobe subdural grid assessments showed right temporal lobe onset. Positron emission tomography was normal. Formal neuropsychometric and Wada procedure demonstrated moderate deficits for declarative memory systems for verbal and nonverbal material. Magnetoencephalography and single photon spectroscopy were not performed. The patient underwent a right anterior temporal lobectomy on February 2012. He was a previously healthy boy without any remarkable medical history. His neurological development was normal. There were no specific epilepsy risk factors including a history of prematurity, head trauma, encephalitis/meningitis, febrile seizures, or family history of epilepsy.

2.2. MR data acquisition

The patient was consented and scanned with a diffusion-weighted sequence in a Siemens 3 T magnet. TR/TE = 15,200/81 ms, 2 images without diffusion weighting, 6 images with b = 100 s/mm^2, and 64 with b = 1000 s/mm^2 and an image resolution of 2 mm isotropic. The diffusion gradients were distributed following an electrostatic repulsion model (Jones et al., 1999). Brain MR imaging demonstrated minimal signal abnormality near the tail the right hippocampus and within the right parahippocampal gyrus. The left hippocampus was grossly normal.

Immediately after the right anterior temporal lobe resection and before tissue fixation, the tissue block was imaged *ex vivo* and fresh at the Advanced Magnetic Resonance Imaging and Spectroscopy (AMRIS) facility of the McKnight Brain Institute at the University of Florida. The tissue was scanned with a diffusion weighted spin echo sequence in a 17.6 T vertical bore magnet (Bruker Corp., Billerica, MA) for 5 h. The tissue was placed in a 20 mm NMR tube (model 20PP, Wilmad-LabGlass, Vineland, NJ) in Flourinert (3 M, St. Paul, MN). The scan parameters were TR/TE = 4000/28 ms, matrix size of 86 × 86 with 75 slices with 220 μm thickness, yielding a final isotropic image resolution of 220 μm. There were a total of 52 diffusion gradients distributed over a sphere following a model

of electrostatic repulsion: 6 gradients with b = 100 s/mm^2 and 46 gradients with b = 2225 s/mm^2. Diffusion mixing time was δ = 3.5 ms and Δ = 17.5 ms.

2.3. Post-processing

Fractional anisotropy and mean diffusivity maps were obtained using in house software. The *ex vivo* acquisition was down-sampled to an image resolution of 1 mm isotropic by using only 19 × 19 k-space points before reconstruction and averaging subsequent slices to achieve a final 1 mm slice thickness. The *in vivo* acquisition was spatially interpolated to 1.0 mm isotropic resolution using cubic convolution (Park and Schowengerdt, 1983) with the CONGRID function in IDL. Matching the spatial resolutions allowed for qualitatively comparisons *in vivo* to *ex vivo* FA maps.

The diffusion displacement probability in each voxel was estimated using a Wishart distribution of diffusion tensors (Jian et al., 2007a,b), this allowed the estimation of multiple fiber orientations per voxel. In this manuscript, the fiber orientations refer to the maxima of the diffusion displacement probability.

2.4. Immunohistochemistry

Tissue blocks were sectioned at 7 micrometer thick with an American Optical 820 microtome. Sections were mounted from 45 °C deionized water on 75 × 38 millimeter slides (Fisher Scientific, Hampton, NH) and dried at 40 °C overnight. Neurofilament proteins were immunolabeled by 45-minute incubation in primary antibody (Cat#MU073-UC, Biogenex, Fremont, CA diluted 1:600 in phosphate buffer solution (PBS)). Sequential 30 minute incubations in biotinylated anti-mouse IgG (Fab specific) (B0529, Sigma Aldrich, St Louis MO, 1:1000 in PBS) and ExtrAvidin® Peroxidase (E2886, Sigma Aldrich, St Louis MO, 1:1000 in PBS) and reaction with 3,3′-diaminobenzidine (DAB, D5637, Sigma Aldrich, St Louis MO; 5 mg of DAB per mL of PBS and 0.4 μL of 30% H_2O_2) was used to visualize immunoreactivity. Sections were counterstained with hematoxylin for contrast between neurofilaments (brown) and cell bodies (purple). Cover-slipped neurofilament immunolabeled sections were examined using conventional bright field illumination on a microscope (Olympus BH-2) connected to a Hitachi KP-D581 color digital video camera relaying images to a desktop computer frame grabber (Integral Tech Spectrim).

Using in-house software developed in IDL (Exelisvis, Boulder, CO), gross anatomical features were used to align MR images with corresponding reference points on tissue sections. An MR slice was selected based on visual inspection to be anatomically similar to the histology sections. Histological sections were registered to the MR slice by visual matching 12–15 fiducial markers (the presence of some features varied across individual sections, Fig. 1). The entorhinal cortex, alveus, angular bundle, dentate gyrus, CA1, CA2, and CA3 sub-fields were used as landmarks to place fiducial markers ensuring an approximate registration of histological images with the MR dataset.

2.5. Tractography

To avoid confusion between fibers from tractography and histology, the term “fibers” will refer to anatomical fibers observed by histology and the term “streamlines” will refer to tractography-derived fiber bundles. Regions of interest (ROI) were manually outlined in fractional anisotropy (FA) maps, using ITK-SNAP (Yushkevich et al., 2006). Probabilistic fiber tracking was performed using FSL’s probtrackx (Behrens et al., 2003), by starting from an anatomical ROI (e.g. dentate gyrus and alveus). Probabilistic tracking parameters were as follows: step-length = 0.1 mm, number of seeds = 5000, curvature threshold = 0.2, maximum number of steps = 2000. Deterministic fiber tracking (Mori et al., 1999) was performed with in-house developed software, written in C, employing the method of Wishart tensor distribution of fiber orientation in each voxel. The deterministic parameters were: step length = 0.1 mm, number of seeds = 125, angle threshold = 70°, low anisotropy stopping criteria (FA < 0.05). Since diffusion is antipodal symmetric, even where known anatomical pathways correlate with streamlines, tractography does not identify efferent or afferent connectivity; it only identifies the cytoarchitectonic organization of the tissue that restricts or hinders water displacement.

In order to obtain the deterministic fiber maps, a fiber density map was created where each voxel value corresponded to the number of streamlines passing through it. The voxels that contained streamlines passing through the hippocampus were used as a mask to eliminate the streamlines that did not pass through the hippocampus.

3. Results

3.1. MR imaging at 3 T

Non-contrast 3 T MR images demonstrated normal brain density, normal gray and white matter differentiation, and normal brain formation. Ventricular size and cisternal/sulcal patterns were appropriate for chronological age. The left hippocampus contralateral to resection appeared normal. Increased T_2 signal was observed around the right amygdala and right hippocampus with secondary hippocampal edema (Fig. 2).

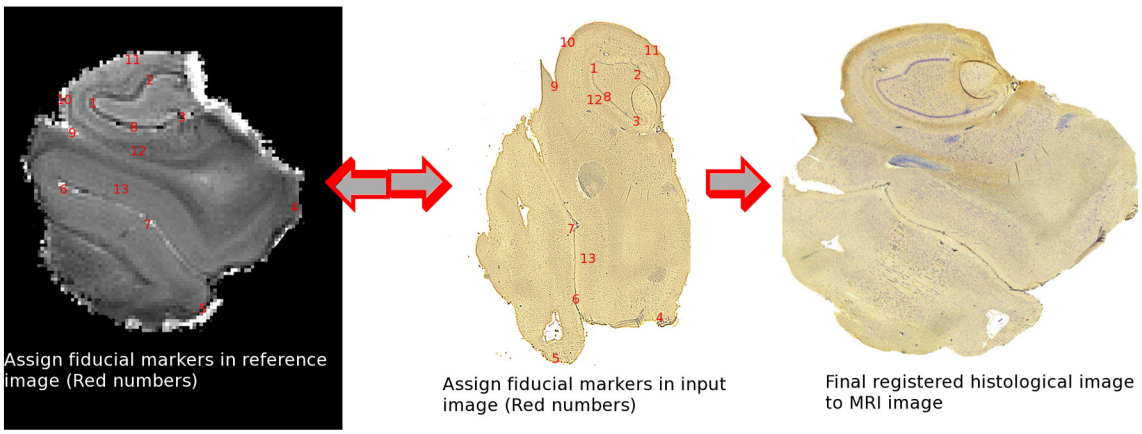

Fig. 1. Registration process from histology slides to MR image space. Landmarks in the MR image are identified and numbered (red numbers in image) and the same landmarks are identified in the original histology image. After non-linear registration the histology image can be overlaid on the MR image to qualitatively associate gray-scale landmarks with histology landmarks.

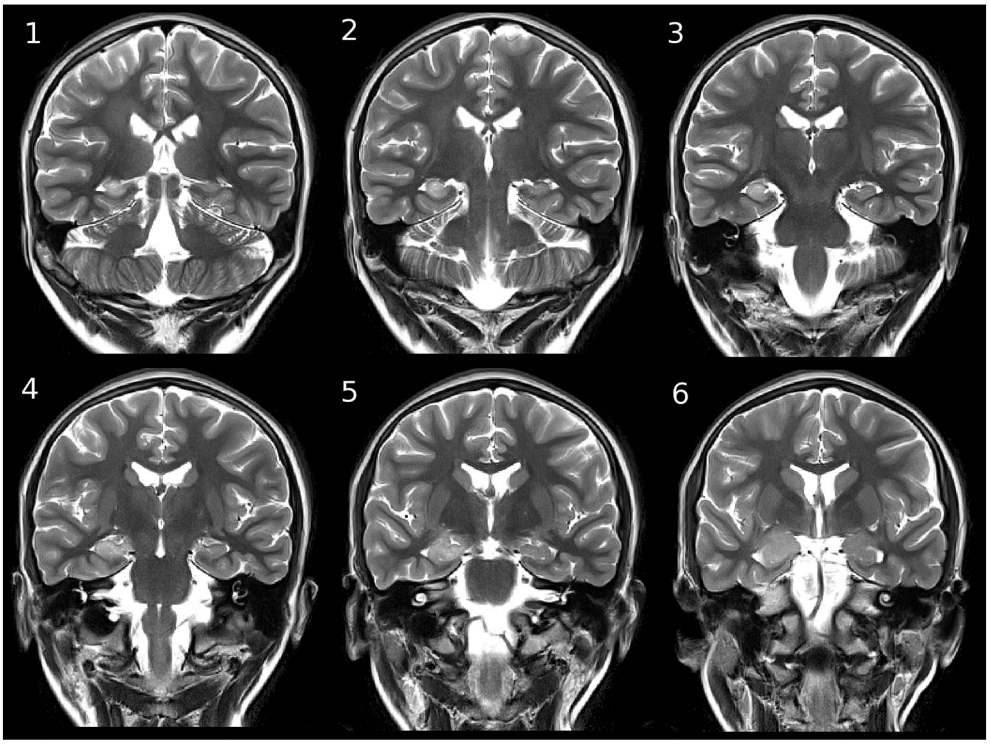

Fig. 2. Clinical *in vivo* T2-weighted image. Higher intensity is observed in right hippocampus (left-side on image) and amygdala. The clinical diagnosis indicated secondary hippocampal edema.

3.2. Clinical histopathology findings

Neuropathology examination of serial sections from rostral levels of the resected hippocampus showed gliosis and multifocal infiltrates of lymphocytes and activated microglial cells forming microglial nodules. Several parenchymal blood vessels contained perivascular cuffs of mature lymphocytes (CD3 and CD45-reactive). Microglial activation in areas of active inflammation was further supported by positive CD68 immunohistochemistry. Astrocytosis was demonstrated by elevated glial fibrillary acidic protein immunohistochemistry. Neuronal loss was detected in hematoxylin/eosin and neurofilament protein immunohistochemistry sections, but was not extensive. In addition, residual neurons of the hippocampus and subiculum showed increased neurofilament protein accumulation.

3.3. In vivo and ex vivo images

The FA map (color coded for fiber orientation) of the *in vivo* acquisition revealed the expected contrast and implied organization and orientation of large white matter structures like the corpus callosum (Fig. 3A). The *in vivo* FA map around the hippocampus area lacked contrast between the alveus and the hippocampus, and also between the hippocampal subregions. In addition, the images exhibited obscured boundaries between the angular bundle, hippocampus, and entorhinal cortex (Fig. 3B). Down-sampling the *ex vivo* images to a 1 mm isotropic resolution presented a slight improvement delineating the temporal lobe structure and the boundaries of the hippocampus, angular bundle and entorhinal cortex. However, no discernable internal structures were seen in this image either (Fig. 3C). Finally, the *ex vivo* high-resolution

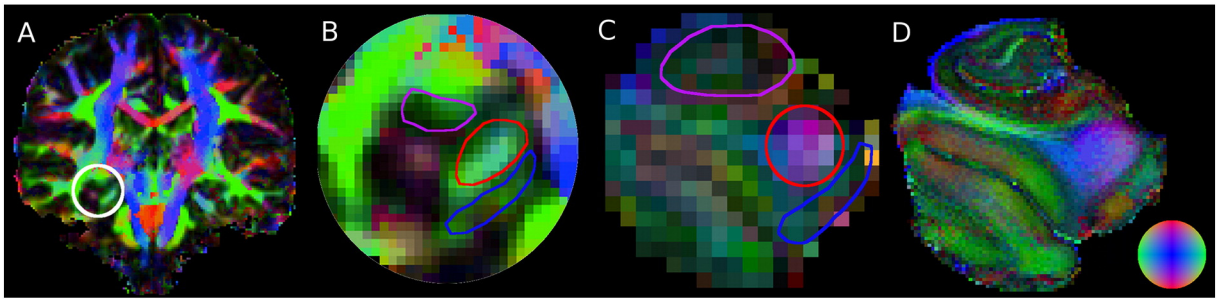

Fig. 3. *Ex vivo-in vivo* comparison of FA map with color reflecting the orientation of the largest maxima of the diffusion displacement probability. (A) Presurgical *in vivo* FA map at 1 mm isotropic spatial resolution reveals macro-scale white matter structures. The color sphere at the bottom right depicts the direction of largest displacement probability orientation. Blue, anterior–posterior; red, superior–inferior; and green, medial-lateral. (B) Enlargement of the white box of (A) illustrates the limited definition of internal features of the temporal lobe. (C) Down-sampled *ex vivo* FA map shows a slightly clearer delineation of the angular bundle, and some definition of the boundaries of the HC not visible in (B). In (B) and (C), the purple oval surround the hippocampus, the red circle surrounds the angular bundle and the blue oval surrounds the entorhinal cortex. (D) Cellular organization can be seen clearly in the high resolution *ex vivo* FA map. White matter structures including the angular bundle and the infrasubicular portion of the alveus are well delineated, as are multiple gray matter subdivisions (e.g. dentate granule cell layer, hippocampus proper, subiculum, and entorhinal cortex).

image (220 micrometer isotropic) obtained at the 17.6 T magnet shows fine details within the hippocampal subregions. Structures like the alveus surrounding the hippocampus were differentiated in exceptional detail (Fig. 3D).

3.4. MR imaging and histology

An anatomical sketch in Fig. 4A shows the approximate boundaries of anatomical subdivisions observed, as described by Duvernoy (1988) in the resected tissue. These structures are also labeled in the average diffusivity map (Fig. 4B). In the histological slides, areas of relatively strong neurofilament immunolabeling within regions such as alveus and granule cell layer (Fig. 4C) corresponded to highly organized regions (i.e hyperintense regions) observed in the FA (Fig. 4D) and dark regions in the average diffusivity map (Fig. 4E). The outer molecular layer appears as a neurofilament dense structure in Fig. 4C, adjacent to the granule cell layer of dentate gyrus, appeared as a bright structure in FA maps and as a distinctive dark band in average diffusivity map. In Fig. 4, the angular bundle and alveus are prominent white matter features but other internal structural boundaries are visible. The alveus, pointed by the red arrow, can be followed from the fimbria along the medial wall of the lateral ventricle, lateral to CA3 and CA1 sub-fields, and continuing inferior to the subiculum (Fig. 4C). The angular bundle displayed mostly a rostral–caudal orientation (Fig. 4F). The color-coded orientation FA maps showed the portion of the alveus ventral to the hippocampus displaying a rostral–caudal orientation, while the dorsal portion displays a medial–lateral orientation (Fig. 4F).

Anatomical features that correlate with diffusion metrics (i.e. FA and average diffusivity) are shown at higher magnification on histology slides in Fig. 5. The outer molecular layer showed a high level of neurofilament architecture dorsal to the granule cell layer (Fig. 5A). A lighter band external to the dark outer molecular layer occupies the location of the hippocampal fissure and stratum moleculare. External to this is a darker band where entorhinal afferents course through CA3-subiculum. The subiculum (SUB, red arrow) is visible inferior to the dentate gyrus, and is bounded ventrally by a white matter band, the alveus (ALV), that is continuous from the fimbria around the medial wall of the lateral ventricle. This WM tract contains fibers of the temporoammonic pathway in addition to other hippocampal afferent and efferent axons. A general cytoarchitectonic organization is observed oriented dorsal-ventral in the subiculum (Fig. 5B, C). This corresponded to the primary apical dendrites of pyramidal neurons in CA1 and subiculum, collectively oriented toward the dentate gyrus (black arrow in Fig. 5D).

The orientation color-coding of Fig. 4F is shown as orientation vectors overlaid in the grayscale FA image in Fig. 6. The organization observed from histology (Fig. 5) agreed with the fiber orientations obtained from the diffusion displacement probabilities (Fig. 6). The fiber orientations in the subiculum and CA1 regions showed a predominant organization parallel to the red arrows (i.e. oriented dorsal-ventral between the alveus and dentate gyrus) (Fig. 6).

3.5. Excised tissue microstructure derived from tractography

The perforant pathway is estimated using probabilistic tractography starting from a region of interest within the entorhinal cortex; streamlines were obtained until they extended to a region of interest in the granule cell layer. Probabilistic streamlines shown in Fig. 7A were initiated from an ROI in the dentate gyrus and ended in an ROI in the entorhinal cortex. Streamlines traversed the alveus and made obtuse turn into the sub-fields of the hippocampus (Fig. 7A, slices 2, 5 and 9). This shows a structural pattern joining the entorhinal cortex to hippocampal subregions. Sections 1–6 show streamlines passing through the subiculum to the dentate gyrus. 7–10, streamlines originating in the

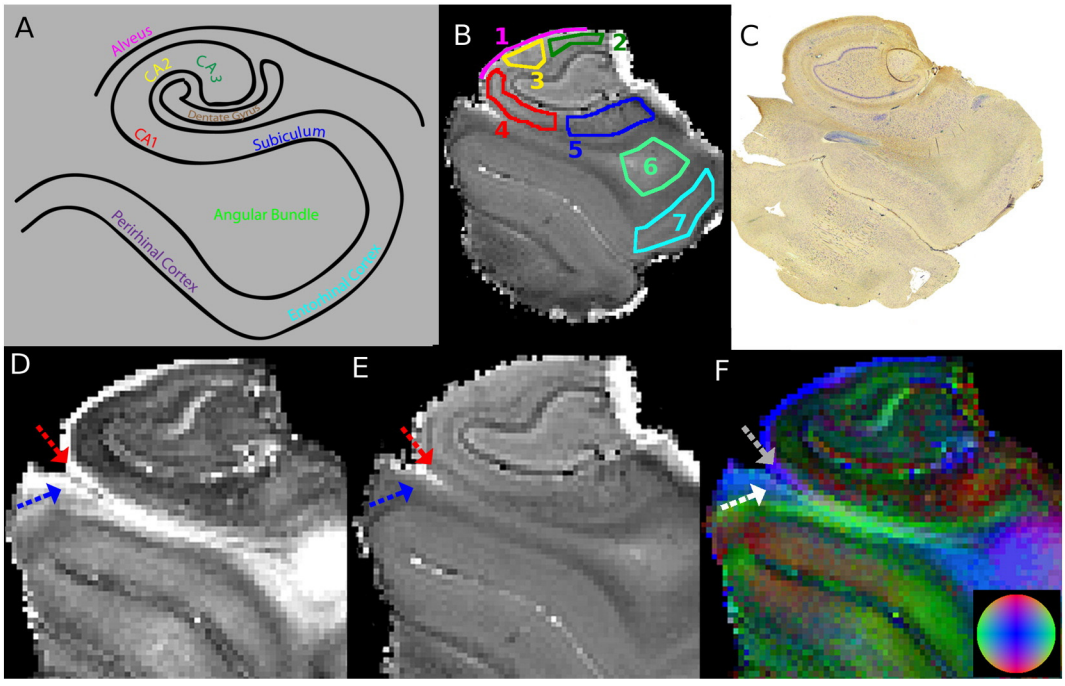

Fig. 4. Anatomical compartments in the resected human temporal lobe according to Duvernoy (1988). (A) Temporal lobe sketch depicting important regions. (B) Average diffusivity map labeled with the subregions of A. The subregions are: 1—fuchsia = alveus, 2—green = CA3, 3—yellow = CA2, 4—red = CA1, 5—blue = subiculum, 6—mint = angular bundle, and 7—turquoise = entorhinal cortex. (C) Histological slide stained for neurofilaments (brown) and cell bodies (purple). (D) Fractional anisotropy (FA) map of *ex vivo* acquisition, arrows point two distinct pathways: one following inferior to CA1 and subiculum from alveus (red arrow in Parts D and E, gray in Part F) and second ventral to the first one following the perirhinal cortex surface (cortical region adjacent to entorhinal cortex, blue arrow in Parts D and E and white in Part F). (E) Average diffusivity map of *ex vivo* acquisition. The tracts dorsal to the hippocampus can be seen as two dark regions separated by a brighter area between them. (F) Orientation FA map, colors represent the direction of the largest maxima obtained by the diffusion displacement probability. The color sphere depicts the direction of largest displacement probability orientation: Blue, anterior–posterior; red, superior–inferior; and green, medial-lateral.

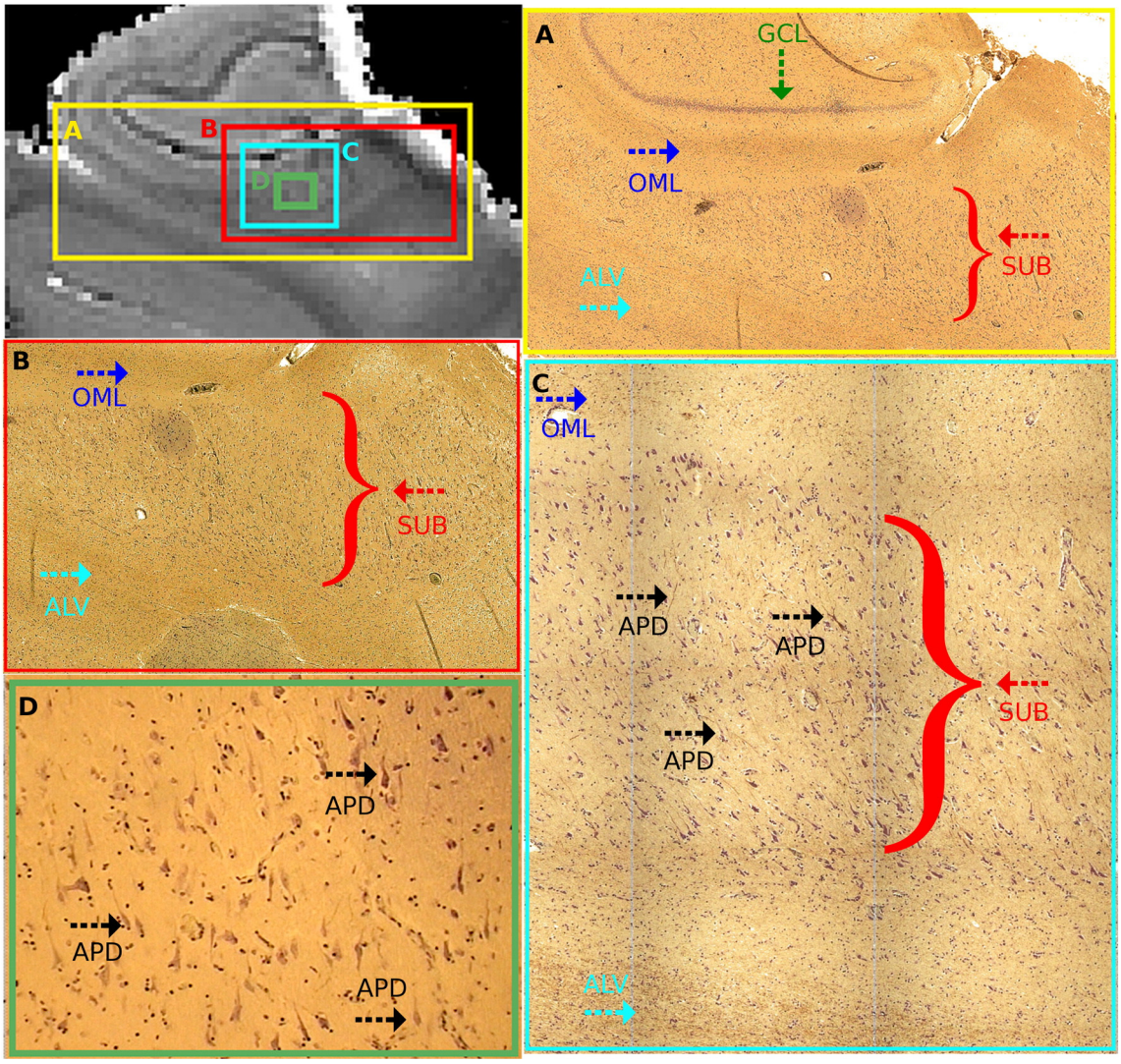

Fig. 5. Microstructure of temporal lobe observed by histological sections. Grayscale image is the average diffusivity (AD) map acquired from the resected sample, displaying boundaries of figures (A–D) and gross anatomical features observed in the histological sections. In the AD image, the dentate granule cell body layer and inner molecular layer (A) correspond to a light band interior to a dark band that appears to correspond to the outer molecular layer. (B) At higher magnification (red box, (B)) regular microstructure begins to emerge, particularly the approximately parallel alignment exhibited by apical dendrites (APD, black arrows in Box C) of subicular pyramidal neurons. The turquoise Box (C) displays these apical dendrites oriented orthogonal to the dentate gyrus, and similar organization of the apical primary dendrites continues throughout CA1 and CA3. The green Box (D), which is the highest magnification of the histological sections, displays the apical dendrites organization parallel to each other in the subiculum. The diffusion measurements also show this organization (this figure).

entorhinal cortex. A second pathway shown in Fig. 7B is made up of streamlines generated from an ROI located in the superior portion of the alveus, which spread out into the rest of the tissue. The alveus can be seen as yellow voxels ventro-lateral to the hippocampus (Fig. 7B, slices 4–8). Streamlines progressed into the CA2 and CA3 regions (Fig. 7B, slices 1–7), and then propagated into the subiculum (Fig. 7B, slices 1–4).

The direct pathway between the entorhinal cortex and hippocampal subfields observed with probabilistic tractography was not observed with the deterministic approach (Fig. 7C–F). The streamlines in Fig.7C, originate from the alveus and propagate into the hippocampus. These are most likely due to mossy fibers and dendritic organization, oriented toward CA3, CA2 and CA1. Streamlines were propagated from an ROI in the angular bundle, displayed a very dense streamline population, and are observed making sharp turns from the dorsal portion of the alveus into the hippocampus. An organized streamline region appeared between the alveus (yellow arrow in Fig. 7D) and the dentate gyrus, through the subiculum and the CA1. The most likely corresponding anatomical feature would be entorhinal cortex axons afferent to the subiculum, hippocampus, and dentate gyrus. The inferior component of the alveus formed a bordering structure of streamlines surrounding the hippocampus from the CA1 up to the subiculum and oriented toward the entorhinal cortex (Fig. 7E). An oblique view of the alveus is shown in Fig. 7F (inferior to hippocampus), portraying a sheet-like structure surrounding the hippocampus by the streamlines dorsal to CA1 and subiculum pointing toward the entorhinal cortex.

4. Discussion

In this work we show results of a freshly resected tissue of a patient undergoing resection due to pharmacological resistant epilepsy. We employ high-field MRI (17.6 T) and tractography (probabilistic and deterministic) to elucidate mesoscale features of temporal lobe anatomy relevant to TLE. Fresh *ex vivo* tissue can also permit complementary physiological analyses currently being employed as a research tool in animal studies (He and Bausch, 2014; Yang et al., 2014) as a method to validate structural findings.

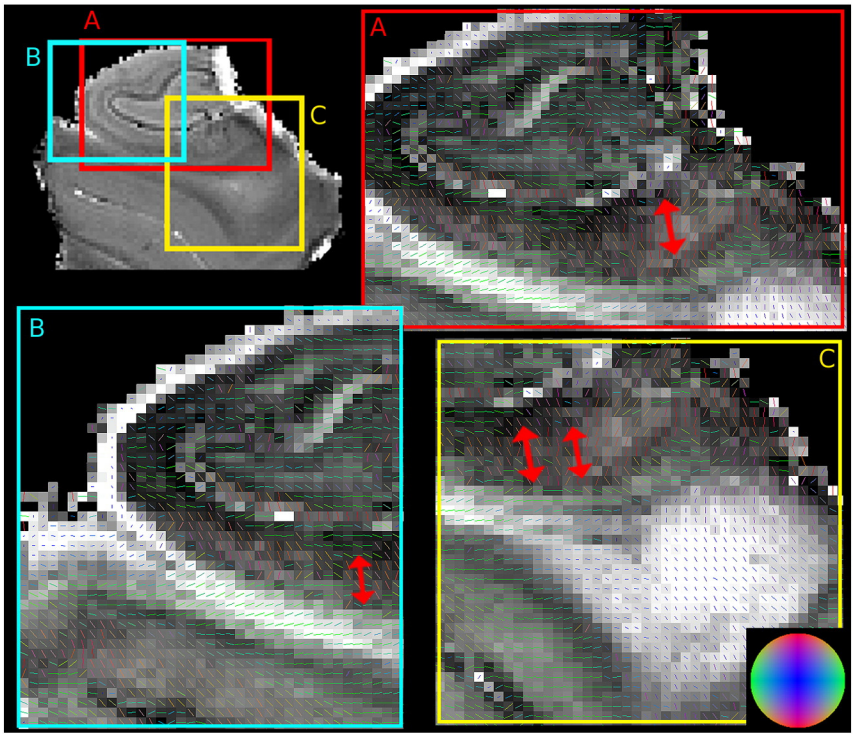

Fig. 6. Microstructural organization of the temporal lobe estimated by diffusion MRI overlayed onto fractional anisotropy maps. Grayscale on top left is the average diffusivity (AD) map displaying the boundaries of the regions displaying fiber orientations obtained by method of Wishart diffusion displacement probability maxima (A–C). (A) Red box displays the hippocampal regions, such as the subiculum and CA1, with largest maxima of water displacement in the direction to and from the dentate gyrus (parallel to red arrow) and the alveus. (B) Turquoise box displays the infra- subicular portion of the alveus traversing horizontally toward the entorhinal cortex. (C) Yellow box displays the angular bundle region with dominant orientation pointing anterior posterior.

4.1. High-field (17.6 T) vs. low-field (3 T) MR imaging

The advantages of using ultra-high field (17.6 T) magnets lie in the capacity to obtain high-resolution images not easily obtained using clinical magnets (e.g. 1.5, 3 or 7 T). It provides information regarding mesoscale structure which in turn allows better interpretations of *in vivo* images, as the one shown in Fig. 1A (Johnson et al., 2002; Shepherd et al., 2007). Comparison between the interpolated *in vivo* acquisition to *ex vivo* down-sampled acquisition at the same spatial resolution of 1 mm isotropic shows that, although the spatial resolution of these two images (Fig. 1B and C) is the same, the contrast and tissue delineation is slightly better in Fig. 3C. The boundary differentiation is improved in the 1 mm isotropic *ex vivo* FA image, as compared to the *in vivo* interpolated FA map. The volume averaging at the interface of tissue and surrounding fluid spaces was minimized since surrounding cerebrospinal fluid is replaced with Fluorinert™, which does not provide any MR signal. The *in vivo* acquisition employs parallel imaging techniques, which reduce the signal-to-noise ratio proportional to the acceleration factor which decrease image quality, and increases artifacts. Each voxel in the *in vivo* MR imaging acquisition (Fig. 3A) corresponded to approximately 750 voxels of the *ex vivo* MR imaging acquisition (Fig. 3D). Voxel volume averaging severely obscured anatomical details visible at 220 μm resolution (Fig. 3). The histological cellular organization shows heterogeneity that cannot be distinguished with 1-millimeter voxel size.

4.2. High resolution MR imaging and histopathology

Detailed anatomical structures were visible in the hippocampal subfields of FA maps and proved suitable for performing a general orientation of the histological sections within the MR dataset. As seen in Fig. 4, the high-resolution MR image shows remarkable differentiation of anatomical regions and correspondence to cellular organization. The FA map shows an improvement in feature recognition with high spatial resolution MR imaging, where two distinct white matter pathways become visible immediately ventral to the CA1 and subiculum (Fig. 4D–F).

Diffusion-tensor MR imaging cannot properly estimate multiple fiber orientations, so high angular resolution diffusion imaging with the method of Wishart calculation of the diffusion displacement probability was used to correlate microstructural features observed in histological slides. The cellular organization of the histology shown in Fig. 5 is properly represented by the displacement probability maxima shown in Fig. 6. The predominant orientation of pyramidal neuron apical dendrites (Fig. 5D) seems to correspond with diffusion maxima orientations in the CA1 and subiculum (Fig. 6A–B). These orientation vectors are not as uniform as implied by the hyperintense regions on the FA map, which would correspond to areas of a single dominating fiber orientation. The non-uniformity of fiber orientations in the subiculum may reflect smaller coherent organization of dendrites compared to bundled axons. In this study, we defined the subiculum broadly; however, it can be differentiated into multiple subcomponents (Ding, 2013; Pluta et al., 2012). The alveus, a white matter tract inferior to the subiculum, displays a medial–lateral organization (Fig. 6B), while the angular bundle displays a rostral–caudal organization (Fig. 6C). Nonetheless, a common feature of the entire subiculum is its apical dendritic organization that will hinder water diffusion in the orientations of the dendrites, as the shown in Fig. 6. Even though this cellular organization (i.e. the brain's microscale) would be difficult to determine with MR, our results show the potential of MR as a marker to determine mesoscale changes within the temporal lobe.

4.3. Temporal lobe structure derived from tractography

Deterministic tractography displays major streamline structures (Fig. 7C–F) that seem to correspond to anatomical landmarks (Fig. 5).

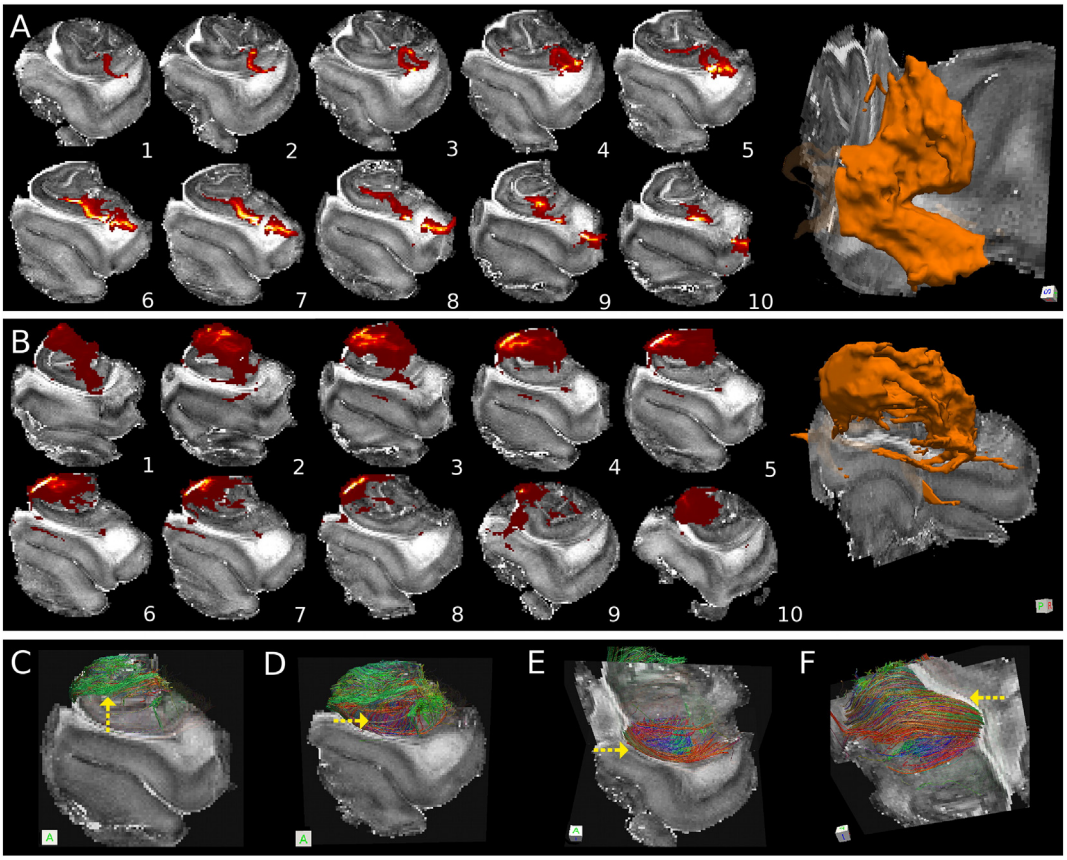

Fig. 7. Three-dimensional visualization of probabilistic and deterministic tractography results. (A) The perforant pathway streamlines compactly traverse through the angular bundle region, and distribute more broadly in the hippocampus and entorhinal cortex. (B) Probabilistic streamlines are obtained starting from a region of interest in the alveus and propagating to the rest of the image with no additional restrictions. The colors correspond to the number of streamlines passing through each voxel, yellow > red. Results were thresholded to display only voxels with 20 or more streamlines. (C–E) 3D streamlines traversing into the hippocampus, estimated by deterministic tractography. Yellow arrows point to streamlines of interest and the bottom left cube denote the orientation of the image. The streamlines in all images are in 3-dimensional space anterior to the slice shown in the background. (C) Coronal view of deterministic streamlines started in the alveus ROI and continued into the hippocampus. (D) Coronal view of streamlines passing through the subiculum and CA1 and extending into the dentate gyrus. (E) Oblique view of alveus (inferior to hippocampus) streamlines pointing to the entorhinal cortex and CA1 traversing inferior to the subiculum. (F) Oblique view of the alveus streamlines shown in (E) traversing inferior to the subiculum creating a sheet of streamlines rounding the inferior part of the hippocampus. In Parts E and F displays a dense, highly organized structure within the subiculum and CA1 region, resembling the general orientation of the apical dendrite organization observed with the immunohistochemistry analysis.

A sheet-like structure, the alveus, surrounds the hippocampus (Fig. 7C–F). This type of detailed information may be used to study changes in fiber tracts and structure in relation to functional disability in neurological diseases. Theoretical analysis of episodic memory (Cheng, 2013) and epilepsy (Goldberg and Coulter, 2013) suggest a connectivity pattern in the temporal lobe that conforms to our tractography estimates of the temporal lobe's microstructural organization. Traditional anatomical descriptions present circuitry in the hippocampal formation (Amaral and Witter, 1989) similar to the one described in Fig. 7. Tractography yields some streamlines that do not appear to have any recognized anatomical significance, but may result from the mixture of directionally coherent axonal structures and dendritic features in the diffusion MR imaging experiments (Fig. 5B slices 1–3 and C). This emphasizes potential limits of MR imaging to study brain organization on the mesoscale level of organization and the need for cautious interpretation based on histological ground truth. In part this is due to the fact that diffusion MR imaging only provides the antipodal symmetric characteristics of water diffusion, preventing MR imaging to detect synaptic connectivity or to imply afferent or efferent fibers.

Probabilistic tractography in contrast to deterministic tractography yields multiple pathways from a single seed point to account for the uncertainty of the fiber orientations (Yamada et al., 2009). High-spatial resolution imaging of *ex vivo* tissue along with tractography may be a useful approach to assay structural integrity of small axonal pathways (Budde and Frank, 2012; Ford et al., 2013; Powell et al., 2012). For example, anterograde tracing studies in primate have shown that axons project from the entorhinal cortex into the dentate gyrus (Amaral et al., 2014). These axons funnel into a tight bundle before dispersing to traverse the subiculum region and penetrate the dentate gyrus. In this work we show a 3-dimensional volume of this pathway is shown in Fig. 7, creating a tight, constrained region at the location of the angular bundle, as seen in the middle slides of Fig. 7, but spreading out in the hippocampus and the entorhinal cortex. Probabilistic tractography shows a streamline pathway (Fig. 7A) similar to this organization, traversing through the angular bundle and then perforating through the subiculum and CA1 toward the dentate molecular layer (Augustinack et al., 2010). This pathway was difficult to discern with histological slides given the heterogeneity of structures along its path (Fig. 3). A secondary pathway is shown propagating from the alveus to the internal subfields of the hippocampus, similar to the pathway obtained by deterministic approach (Fig. 7C). This second pathway does not traverse the complicated trajectory of the first one, therefore it is easily observed with both schemes.

4.4. Clinical implications and future applications

Tissue degradation due to 4 h the fresh tissue was in the magnet during imaging was not observed in the clinical histological assessment,

which makes it possible to extend the battery of studies to include the measurement of streamline fibrous pathways obtained from tractography and compare this with the results of electrical stimulation (Bucci et al., 2013; Feasey et al., 1986). The imaging methods used in this study, with the proper controls in the experimental procedures, may assist in the determination of mesoscale changes resulting from neurological disorders. All this is limited by the availability of tissue and practical subtleties of performing these experiments.

In vivo schemes that employ sub-millimeter in-plane resolution to study changes within the temporal lobe usually use large slice thickness (>3 mm) (Yassa et al., 2010). With these MR schemes, the large thick slices average the complexity within the region into a single gray scale DWI value. Hence, changes observed within large voxels cannot be attributed to a single microscopic pathway, but reflects instead the changes in the organization of all the structures within the region under study. In contrast, the results presented in this study reveal the heterogeneity of structures and sources of DWI contrast (i.e. tractography) within the hippocampus. In this way, ex vivo high spatial resolution measurements allow the study of individual pathways smaller than can be observed with in vivo imaging.

MR imaging is commonly used to guide deep brain stimulation (McIntyre et al., 2015) and epilepsy surgeries (Tax et al., 2014). Techniques that require pre-surgical anatomical scans are preferred by deep-brain-stimulation surgery patients because the techniques provide greater comfort without sacrificing surgical efficacy (Holloway et al., 2005). A problem with this approach is the difficulty of implementing these techniques on small target areas with low contrast anatomical in the MR images. In epilepsy, pre-surgical planning using tractography is restricted to large white matter structures. The approach presented in this manuscript can be used to develop location probability maps in population cohorts (Keren et al., 2009), which may enhance the effectiveness of diffusion MR imaging to assist in surgical planning (Tax et al., 2014). The present *ex vivo* protocol, in a larger patient cohort, could provide the impetus to employ this histopathology/diffusion-MR imaging/tractography analyses approach to improve interventional MR imaging surgeries. These studies have the potential to help set gold standards that could improve surgical procedures.

4.5. Study limitations

The major limitations of this MR imaging approach are the long acquisition times (~5 h compared to <20 min for *in vivo* acquisition) and limited space by the coil diameter in the 17.6 T magnet (samples smaller than 20 mm in diameter). The medial portions of the temporal lobe were not excised in the surgery, which made the coil size ideal for the tissue provided. However, similar *ex vivo* (fixed tissue) studies have performed high-resolution sub-millimeter image resolution (not isotropic) with acquisition time of >15 h (Coras et al., 2014). The relatively fast acquisition of 5 h of *ex vivo* tissue allows us to perform future electrophysiological recordings of the resected tissue not possible with more prolonged post mortem intervals. However, with proper planning (transferring the tissue from the surgery room to the MRI suite and back to pathology laboratory) these would not pose major issues hindering the future application of the methods presented in this article.

Using these methods for other regions (e.g. thalamus, brain stem, among others) would be determined by tissue sample size and feasibility to obtain intact tissue from the surgery. Considering the ex vivo tissue aspect (regardless whether it is fresh tissue or fixed from cadavers), the size will determine the coil and magnet that should be employed. The 17.6 T magnet will hold up samples to about 30 mm in diameter. However in an 11.1 T with a gradient system of 120 mm in diameter we can employ a coil that can probe samples up to 50 mm in diameter. The examples mentioned employ a volume coil for better homogeneity; however, increasing coil diameter reduces the signal to noise ratio hence making such acquisition more difficult. Proper planning can enable similar quality results as the ones presented here.

5. Conclusion

This study employed 17.6 T magnets and high resolution diffusion MR imaging methods to characterize the cytoarchitectonic features of the human hippocampus and surrounding area, as well as trace pathways of small tracts at micrometer MR resolution that is not possible with lower-field *in vivo* MR imaging. Using 17.6 T imaging and sub-millimeter imaging spatial resolution, the organization obtained by tractography showed a level of complexity within the temporal lobe far beyond that attainable with clinical *in vivo* acquisition MR imaging. Indeed, *in vivo* diffusion MR imaging yields insufficient structural information from substructures of the temporal lobe. *Ex vivo* MR imaging from recently resected tissue and before fixation yields additional information about internal structures of the temporal lobe that may be diagnostically or prognostically useful. Diffusion scalar maps including FA and AD maps of fresh tissue resembled the cytoarchitectural organization observed only with thin slice histology. The diffusion displacement probabilities also correlated with the main directional organization of either axonal projection systems or dendrites. The complex features of the temporal lobe are confounded and voxel-averaged at millimeter resolutions (>1 mm). These techniques could be employed in a study of multiple samples to potentially identify in excised tissue areas of major damage related to disease, which could aid histopathology examinations and surgical planning. Ultimately, the proliferation of high-field *ex vivo* studies can lead to a broader understanding of the relationship between pathological states and structural changes in the brain, which could increase our knowledge and lead to improved clinical assessments and outcomes for patients. Our protocol may help further disentangling of pathogenic mechanisms by identifying sites vulnerable to epilepsy. These innovations promise increased sensitivity to the detection of markers of many epileptic diseases and syndromes. Our protocol may help further elucidate the pathogenic mechanisms of epilepsy by identifying sites vulnerable to change not visible with current clinical MR imaging. For example, evidence for structural connectivity patterns within the medial temporal lobe is derived primarily from post-mortem histological studies. In humans and non-human primates, the parahippocampal gyrus and their efferent projections to the entorhinal cortex are distinct. Until recently, these neural circuits could not be visualized in vivo. Development of ex vivo high-field MRI and analytic software applications now allows segmentation of gray matter structures based on their connectivity patterns. In line with histology results, MR imaging connectivity-based parcellation showed clearly defined distinct regions within the entorhinal cortex connecting to perirhinal and hippocampus. The implications for relating such results to neuropsychometric analyses advance understanding about changes in limbic connectivity and how this relates to memory and cognitive deficits. Also the approach used in this study allows detailed three-dimensional reconstruction of the entire intact resected tissue sample. This approach could also help to identify changes in hippocampal subfields and association tracks that have been implicated in epilepsy, such as loss of CA3 and dentate gyrus in the case of mesial temporal lobe sclerosis, or loss of association fibers (Shaffer collaterals) and mossy fiber sprouting, or loss of hippocampal inputs (perforant pathway) and outputs (fornix, subiculum) which have been shown to be early markers of epileptogenesis. In summary, detailed understanding of temporal lobe anatomy, and specifically identifying changes in structure through high field brain MR imaging, may help provide a better understand of the structural contributions to the human epileptic process, associated language and memory deficits, which in turn will aid with medical management of the individual.

Acknowledgments

The support for this work was provided by the B.J. and Eve Wilder Center of Excellence for Epilepsy Research, NINDS National Institutes of Health grant RO1 NS063360, and the North Florida/South Georgia

Veterans Health System, Gainesville, FL. The contents do not represent the views of the U.S Department of Veterans Affairs or the United States Government. The authors would like to thank: Dr. Anthony Yachnis (University of Florida Neuropathology Department) for insightful discussions regarding the immunohistochemistry planning, Dr. Steven N. Roper (University of Florida Department of Neurosurgery), who performed the temporal lobe resection, and Dr. Ronald Quisling (University of Florida Radiology Department), who provided the *in vivo* MR images for comparison. A portion of this work was performed in the McKnight Brain Institute at the National High Magnetic Field Laboratory's AMRIS Facility, which is supported by National Science Foundation Cooperative Agreement No. DMR-1157490, the State of Florida, and the U.S. Department of Energy. The authors would also like to thanks Prof. Marcelo Febo (University of Florida Department of Psychiatry) for insightful discussions regarding the final manuscript. The contents of this paper do not represent the views of the U.S. Department of Veterans Affairs, Department of Defense or the United States Government.

References

Amaral, D.G., Kondo, H., Lavenex, P., 2014. An analysis of entorhinal cortex projections to the dentate gyrus, hippocampus, and subiculum of the neonatal macaque monkey. J. Comp. Neurol. 522 (7), 1485–1505. http://dx.doi.org/10.1002/cne.23469241226445.

Amaral, D.G., Witter, M.P., 1989. The three-dimensional organization of the hippocampal formation: a review of anatomical data. Neuroscience 31 (3), 571–591. http://dx.doi.org/10.1016/0306-4522(89)90424-72687721.

Augustinack, J.C., Helmer, K., Huber, K.E., Kakunoori, S., Zöllei, L., Fischl, B., 2010. Direct visualization of the perforant pathway in the human brain with ex vivo diffusion tensor imaging. Front. Hum. Neurosci. 4, 42. http://dx.doi.org/10.3389/fnhum.2010.0004220577631.

Bauer, J., Burr, W., 2001. Course of chronic focal epilepsy resistant to anticonvulsant treatment. Seizure 10 (4), 239–246. http://dx.doi.org/10.1053/seiz.2000.049911466018.

Beaulieu, C., 2002. The basis of anisotropic water diffusion in the nervous system — a technical review. N.M.R. Biomed. 15 (7–8), 435–455. http://dx.doi.org/10.1002/nbm.78212489094.

Behrens, T.E., Woolrich, M.W., Jenkinson, M., Johansen-Berg, H., Nunes, R.G., Clare, S., Matthews, P.M., Brady, J.M., Smith, S.M., 2003. Characterization and propagation of uncertainty in diffusion-weighted MR imaging. Magn. Reson. Med. 50 (5), 1077–1088. http://dx.doi.org/10.1002/mrm.1060914587019.

Bronen, R.A., Fulbright, R.K., King, D., Kim, J.H., Spencer, S.S., Spencer, D.D., Lange, R.C., 1997. Qualitative MR imaging of refractory temporal lobe epilepsy requiring surgery: correlation with pathology and seizure outcome after surgery. A.J.R. Am. J. Roentgenol. 169 (3), 875–882. http://dx.doi.org/10.2214/ajr.169.3.92759159275915.

Bucci, M., Mandelli, M.L., Berman, J.I., Amirbekian, B., Nguyen, C., Berger, M.S., Henry, R.G., 2013. Quantifying diffusion MRI tractography of the corticospinal tract in brain tumors with deterministic and probabilistic methods. Neuroimage Clin. 3, 361–368. http://dx.doi.org/10.1016/j.nicl.2013.08.00824273719.

Budde, M.D., Frank, J.A., 2012. Examining brain microstructure using structure tensor analysis of histological sections. Neuroimage 63 (1), 1–10. http://dx.doi.org/10.1016/j.neuroimage.2012.06.04222759994.

Cadotte, A.J., Mareci, T.H., DeMarse, T.B., Parekh, M.B., Rajagovindan, R., Ditto, W.L., Talathi, S.S., Hwang, D.U., Carney, P.R., 2009. Temporal lobe epilepsy: anatomical and effective connectivity. I.E.E.E. Trans. Neural Syst. Rehabil. Eng. 17 (3), 214–223. http://dx.doi.org/10.1109/TNSRE.2008.20062201927304O.

Cammoun, L., Gigandet, X., Meskaldji, D., Thiran, J.P., Sporns, O., Do, K.Q., Maeder, P., Meuli, R., Hagmann, P., 2012. Mapping the human connectome at multiple scales with diffusion spectrum MRI. J. Neurosci. Methods 203 (2), 386–397. http://dx.doi.org/10.1016/j.jneumeth.2011.09.03122001222.

Cheng, S., 2013. The CRISP theory of hippocampal function in episodic memory. Front. Neural Circuits 7, 88. http://dx.doi.org/10.3389/fncir.2013.0008823653597.

Concha, L., Beaulieu, C., Collins, D.L., Gross, D.W., 2009. White-matter diffusion abnormalities in temporal-lobe epilepsy with and without mesial temporal sclerosis. J. Neurol. Neurosurg. Psychiatry 80 (3), 312–319. http://dx.doi.org/10.1136/jnnp.2007.13928718977826.

Concha, L., Beaulieu, C., Gross, D.W., 2005. Bilateral limbic diffusion abnormalities in unilateral temporal lobe epilepsy. Ann. Neurol. 57 (2), 188–196. http://dx.doi.org/10.1002/ana.2033415562425.

Coras, R., Milesi, G., Zucca, I., Mastropietro, A., Scotti, A., Figini, M., Mühlebner, A., Hess, A., Graf, W., Tringali, G., Blümcke, I., Villani, F., Didato, G., Frassoni, C., Spreafico, R., Garbelli, R., 2014. 7 T MRI features in control human hippocampus and hippocampal sclerosis: an ex vivo study with histologic correlations. Epilepsia. Epilepsia 55 (12), 2003–2016. http://dx.doi.org/10.1111/epi.1282825366369.

Ding, S.L., 2013. Comparative anatomy of the prosubiculum, subiculum, presubiculum, postsubiculum, and parasubiculum in human, monkey, and rodent. J. Comp. Neurol. 521 (18), 4145–4162. http://dx.doi.org/10.1002/cne.2341623839777.

Duvernoy, H.M., 1988. The Human Hippocampus: An Atlas of Applied Anatomy. J.F. Bergmann Verlag, Munich.

Eichenbaum, H., Sauvage, M., Fortin, N., Komorowski, R., Lipton, P., 2012. Towards a functional organization of episodic memory in the medial temporal lobe. Neurosci. Biobehav. Rev. 36 (7), 1597–1608. http://dx.doi.org/10.1016/j.neubiorev.2011.07.00621810443.

Eichenbaum, H., Yonelinas, A.P., Ranganath, C., 2007. The medial temporal lobe and recognition memory. Annu. Rev. Neurosci. 30, 123–152. http://dx.doi.org/10.1146/annurev.neuro.30.051606.09432817417939.

England, M.J., Liverman, C.T., Schultz, A.M., Strawbridge, L.M., 2012. Epilepsy across the spectrum: promoting health and understanding. A summary of the Institute of Medicine report. Epilepsy Behav. 25 (2), 266–276. http://dx.doi.org/10.1016/j.yebeh.2012.06.01623041175.

Feasey, K.J., Lynch, M.A., Bliss, T.V.S., 1986. Long-term potentiation is associated with an increase in calcium-dependent, potassium-stimulated release of [^{14}C]glutamate from hippocampal slices: an ex vivo study in the rat. Brain Research 364 (1), 39–44. http://dx.doi.org/10.1016/0006-8993(86)90985-6.

Ford, A.A., Colon-Perez, L., Triplett, W.T., Gullett, J.M., Mareci, T.H., Fitzgerald, D.B., 2013. Imaging white matter in human brainstem. Front Hum Neurosci 7, 400. http://dx.doi.org/10.3389/fnhum.2013.0040023898254.

Gerdes, J.S., Walther, E.U., Jaganjac, S., Makrigeorgi-Butera, M., Meuth, S.G., Deppe, M., 2014. Early detection of widespread progressive brain injury after cardiac arrest: a single case DTI and post-mortem histology study. PLOS One 9 (3), e92103. http://dx.doi.org/10.1371/journal.pone.009210324633135.

Goldberg, E.M., Coulter, D.A., 2013. Mechanisms of epileptogenesis: a convergence on neural circuit dysfunction. Nat. Rev. Neurosci. 14 (5), 337–349. http://dx.doi.org/10.1038/nrn348223595016.

Gross, D.W., 2011. Diffusion tensor imaging in temporal lobe epilepsy. Epilepsia 52 (Suppl. 4), 32–34. http://dx.doi.org/10.1111/j.1528-1167.2011.03149.x21732939.

Hagmann, P., Cammoun, L., Gigandet, X., Meuli, R., Honey, C.J., Wedeen, V.J., Sporns, O., 2008. Mapping the structural core of human cerebral cortex. PLOS Biol. 6 (7), e159. http://dx.doi.org/10.1371/journal.pbio.006015918597554.

Hagmann, P., Jonasson, L., Maeder, P., Thiran, J.P., Wedeen, V.J., Meuli, R., 2006. Understanding diffusion MR imaging techniques: from scalar diffusion-weighted imaging to diffusion tensor imaging and beyond. RadioGraphics 26 (Suppl. 1), S205–S223. http://dx.doi.org/10.1148/rg.26si06551017050517.

He, S., Bausch, S.B., 2014. Synaptic plasticity in glutamatergic and GABAergic neurotransmission following chronic memantine treatment in an in vitro model of limbic epileptogenesis. Neuropharmacology 77, 379–386. http://dx.doi.org/10.1016/j.neuropharm.2013.10.01624184417.

Holloway, K.L., Gaede, S.E., Starr, P.A., Rosenow, J.M., Ramakrishnan, V., Henderson, J.M., 2005. Frameless stereotaxy using bone fiducial markers for deep brain stimulation. J. Neurosurg. 103 (3), 404–413. http://dx.doi.org/10.3171/jns.2005.103.3.040416235670.

Jian, B., Vemuri, B.C., Ozarslan, E., Carney, P., Mareci, T., 2007a. A continuous mixture of tensors model for diffusion-weighted MR signal reconstruction. Proc IEEE Int Symp Biomed Imaging 4, 772–775.

Jian, B., Vemuri, B.C., Ozarslan, E., Carney, P.R., Mareci, T.H., 2007b. A novel tensor distribution model for the diffusion-weighted MR signal. NeuroImage 37 (1), 164–176. http://dx.doi.org/10.1016/j.neuroimage.2007.03.07417570683.

Johnson, G.A., Calabrese, E., Little, P.B., Hedlund, L., Qi, Y., Badea, A., 2014. Quantitative mapping of trimethyltin injury in the rat brain using magnetic resonance histology. Neurotoxicology 42, 12–23. http://dx.doi.org/10.1016/j.neuro.2014.02.00924631313.

Johnson, G.A., Cofer, G.P., Fubara, B., Gewalt, S.L., Hedlund, L.W., Maronpot, R.R., 2002. Magnetic resonance histology for morphologic phenotyping. J. Magn. Reson. Imaging 16 (4), 423–429. http://dx.doi.org/10.1002/jmri.1017512353257.

Jones, D.K., Horsfield, M.A., Simmons, A., 1999. Optimal strategies for measuring diffusion in anisotropic systems by magnetic resonance imaging. Magn. Reson. Med. 42 (3), 515–52510467296.

Keren, N.I., Lozar, C.T., Harris, K.C., Morgan, P.S., Eckert, M.A., 2009. In vivo mapping of the human locus coeruleus. Neuroimage 47 (4), 1261–1267. http://dx.doi.org/10.1016/j.neuroimage.2009.06.01219524044.

Kienzler, F., Norwood, B.A., Sloviter, R.S., 2009. Hippocampal injury, atrophy, synaptic reorganization, and epileptogenesis after perforant pathway stimulation-induced status epilepticus in the mouse. J. Comp. Neurol. 515 (2), 181–196. http://dx.doi.org/10.1002/cne.2205919412934.

Liao, W., Ding, J., Marinazzo, D., Xu, Q., Wang, Z., Yuan, C., Zhang, Z., Lu, G., Chen, H., 2011a. Small-world directed networks in the human brain: multivariate Granger causality analysis of resting-state fMRI. Neuroimage 54 (4), 2683–2694. http://dx.doi.org/10.1016/j.neuroimage.2010.11.00721073960.

Liao, W., Zhang, Z., Pan, Z., Mantini, D., Ding, J., Duan, X., Luo, C., Wang, Z., Tan, Q., Lu, G., Chen, H., 2011b. Default mode network abnormalities in mesial temporal lobe epilepsy: a study combining fMRI and DTI. Hum. Brain Mapp. 32 (6), 883–895. http://dx.doi.org/10.1002/hbm.2107620533558.

Liu, M., Chen, Z., Beaulieu, C., Gross, D.W., 2014. Disrupted anatomic white matter network in left mesial temporal lobe epilepsy. Epilepsia 55 (5), 674–682. http://dx.doi.org/10.1111/epi.1258124650167.

Liu, M., Concha, L., Lebel, C., Beaulieu, C., Gross, D.W., 2012. Mesial temporal sclerosis is linked with more widespread white matter changes in temporal lobe epilepsy. Neuroimage Clin. 1 (1), 99–105. http://dx.doi.org/10.1016/j.nicl.2012.09.01024179742.

McIntyre, C.C., Chaturvedi, A., Shamir, R.R., Lempka, S.F., 2015. Engineering the next generation of clinical deep brain stimulation technology. Brain Stimul. 8 (1), 21–26. http://dx.doi.org/10.1016/j.brs.2014.07.03925161150.

Mori, S., Crain, B.J., Chacko, V.P., van Zijl, P.C., 1999. Three-dimensional tracking of axonal projections in the brain by magnetic resonance imaging. Ann. Neurol. 45 (2), 265–269. http://dx.doi.org/10.1002/1531-8249(199902)45:2<265::AID-ANA21>3.0.CO;2-39989633.

Oh, S.W., Harris, J.A., Ng, L., Winslow, B., Cain, N., Mihalas, S., Wang, Q., Lau, C., Kuan, L., Henry, A.M., Mortrud, M.T., Ouellette, B., Nguyen, T.N., Sorensen, S.A., Slaughterbeck, C.R., Wakeman, W., Li, Y., Feng, D., Ho, A., Nicholas, E., Hirokawa, K.E., Bohn, P., Joines, K.M., Peng, H., Hawrylycz, M.J., Phillips, J.W., Hohmann, J.G., Wohnoutka, P., Gerfen, C.R., Koch, C., Bernard, A., Dang, C., Jones, A.R., Zeng, H., 2014. A mesoscale connectome of the mouse brain. Nature 508 (7495), 207–214. http://dx.doi.org/10.1038/nature1318624695228.

Parekh, M.B., Carney, P.R., Sepulveda, H., Norman, W., King, M., Mareci, T.H., 2010. Early MR diffusion and relaxation changes in the parahippocampal gyrus precede the onset of spontaneous seizures in an animal model of chronic limbic epilepsy. Exp. Neurol. 224 (1), 258–270. http://dx.doi.org/10.1016/j.expneurol.2010.03.03120394745.

Park, S.K., Schowengerdt, R.A., 1983. Image reconstruction by parametric cubic convolution. Comput. Vis. Graph. Image Process. 23 (3), 258–272. http://dx.doi.org/10.1016/0734-189X(83)90026-9.

Pluta, J., Yushkevich, P., Das, S., Wolk, D., 2012. In vivo analysis of hippocampal subfield atrophy in mild cognitive impairment via semi-automatic segmentation of T2-weighted MRI. J. Alzheimers Dis. 31 (1), 85–99. http://dx.doi.org/10.3233/JAD-2012-11193122504319.

Powell, M.H., Nguyen, H.V., Gilbert, M., Parekh, M., Colon-Perez, L.M., Mareci, T.H., Montie, E., 2012. Magnetic resonance imaging and volumetric analysis: novel tools to study the effects of thyroid hormone disruption on white matter development. Neurotoxicology 33 (5), 1322–1329. http://dx.doi.org/10.1016/j.neuro.2012.08.00822975424.

Shepherd, T.M., Ozarslan, E., Yachnis, A.T., King, M.A., Blackband, S.J., 2007. Diffusion tensor microscopy indicates the cytoarchitectural basis for diffusion anisotropy in the human hippocampus. A.J.N.R. Am. J. Neuroradiol. 28 (5), 958–9617494678.

Silasi, G., Murphy, T.H., 2014. Stroke and the connectome: how connectivity guides therapeutic intervention. Neuron 83 (6), 1354–1368. http://dx.doi.org/10.1016/j.neuron.2014.08.05225233317.

Sporns, O., Tononi, G., Kötter, R., 2005. The human connectome: a structural description of the human brain. PLOS Comput. Biol. 1 (4), e42. http://dx.doi.org/10.1371/journal.pcbi.001004216201007.

Sutula, T., Cascino, G., Cavazos, J., Parada, I., Ramirez, L., 1989. Mossy fiber synaptic reorganization in the epileptic human temporal lobe. Ann. Neurol. 26 (3), 321–330. http://dx.doi.org/10.1002/ana.4102603032508534.

Tax, C.M., Duits, R., Vilanova, A., Ter Haar Romeny, B.M., Hofman, P., Wagner, L., Leemans, A., Ossenblok, P., 2014. Evaluating contextual processing in diffusion MRI: application to optic radiation reconstruction for epilepsy surgery. PLOS One 9 (7). http://dx.doi.org/10.1371/journal.pone.010152425077946.

Wisse, L.E., Gerritsen, L., Zwanenburg, J.J., Kuijf, H.J., Luijten, P.R., Biessels, G.J., Geerlings, M.I., 2012. Subfields of the hippocampal formation at 7 T MRI: in vivo volumetric assessment. Neuroimage 61 (4), 1043–1049. http://dx.doi.org/10.1016/j.neuroimage.2012.03.02322440643.

Yamada, K., Sakai, K., Akazawa, K., Yuen, S., Nishimura, T., 2009. MR tractography: a review of its clinical applications. Magn. Reson. Med. Sci. 8 (4), 165–174. http://dx.doi.org/10.2463/mrms.8.16520035125.

Yang, S., Yang, S., Moreira, T., Hoffman, G., Carlson, G.C., Bender, K.J., Alger, B.E., Tang, C.M., 2014. Interlamellar CA1 network in the hippocampus. Proc. Natl. Acad. Sci. U. S. A. 111 (35), 12919–12924. http://dx.doi.org/10.1073/pnas.140546811125139992.

Yassa, M.A., Muftuler, L.T., Stark, C.E., 2010. Ultrahigh-resolution microstructural diffusion tensor imaging reveals perforant path degradation in aged humans in vivo. Proc. Natl. Acad. Sci. U. S. A. 107 (28), 12687–12691. http://dx.doi.org/10.1073/pnas.100211310720616040.

Yushkevich, P.A., Piven, J., Hazlett, H.C., Smith, R.G., Ho, S., Gee, J.C., Gerig, G., 2006. User-guided 3D active contour segmentation of anatomical structures: significantly improved efficiency and reliability. Neuroimage 31 (3), 1116–1128. http://dx.doi.org/10.1016/j.neuroimage.2006.01.01516545965.

Yushkevich, P.A., Wang, H., Pluta, J., Das, S.R., Craige, C., Avants, B.B., Weiner, M.W., Mueller, S., 2010. Nearly automatic segmentation of hippocampal subfields in in vivo focal T2-weighted MRI. Neuroimage 53 (4), 1208–1224. http://dx.doi.org/10.1016/j.neuroimage.2010.06.04020600984.